

TITLE

- AADS: Augmented Autonomous Driving Simulation using Data-driven Algorithms
- Augmented Autonomous Driving Simulation

Authors

W. Li,^{1*}† C. W. Pan,^{2*} R. Zhang,^{3*} J. P. Ren,³ Y. X. Ma,⁴ J. Fang,¹ F. L. Yan,¹ Q. C. Geng,⁵ X. Y. Huang,¹ H. J. Gong,⁶ W. W. Xu,³ G. P. Wang,² D. Manocha,⁷† R. G. Yang^{1†}

Affiliations

- 1, Baidu Research, Beijing, China
- 2, Peking University, Beijing, China
- 3, Zhejiang University, Hangzhou, China
- 4, The University of Hong Kong, Hongkong, China
- 5, Beihang University, Beijing, China
- 6, Nanjing University of Aeronautics and Astronautics, Nanjing, China
- 7, University of Maryland, College Park, USA

* These authors contributed equally to this work.

† Corresponding authors. Emails: {liwei87, yangruigang}@baidu.com, dm@cs.umd.edu.

Abstract

Simulation systems have become an essential component in the development and validation of autonomous driving technologies. The prevailing state-of-the-art approach for simulation is to use game engines or high-fidelity computer graphics (CG) models to create driving scenarios. However, creating CG models and vehicle movements (e.g., the assets for simulation) remains a manual task that can be costly and time-consuming. In addition, the fidelity of CG images still lacks the richness and authenticity of real-world images and using these images for training leads to degraded performance.

In this paper we present a novel approach to address these issues: Augmented Autonomous Driving Simulation (AADS). Our formulation augments real-world pictures with a simulated traffic flow to create photo-realistic simulation images and renderings. More specifically, we use LiDAR and cameras to scan street scenes. From the acquired trajectory data, we generate highly plausible traffic flows for cars and pedestrians and compose them into the background. The composite images can be re-synthesized with different viewpoints and sensor models (camera or LiDAR). The resulting images are photo-realistic, fully annotated, and ready for end-to-end training and testing of autonomous driving systems from perception to planning. We explain our system design and validate our algorithms with a number of autonomous driving tasks from detection to segmentation and predictions.

Compared to traditional approaches, our method offers unmatched scalability and realism. Scalability is particularly important for AD simulation and we believe the complexity and diversity of the real world cannot be realistically captured in a virtual environment. Our augmented approach combines the flexibility in a virtual environment (e.g., vehicle movements) with the richness of the real world to allow effective simulation of anywhere on earth.

Summary

By augmenting images with synthesized traffic, we present a truly scalable and high-fidelity simulation system to enable end-to-end training/testing of autonomous driving anywhere on earth.

MAIN TEXT

1. Introduction

Autonomous vehicles (AV) have attracted a lot of attention in the last few years from researchers, venture capitalists, and the general public. The societal benefits in terms of safety, mobility, and environmental concerns are expected to be tremendous and have captivated the attentions of people across the globe. However, in light of recent accidents involving AV, it has become clear that there is still a long way to go to meet the high standards and expectations associated with AV.

Safety is the key requirement for AV. It has been argued that an AV has to be test-driven hundreds of millions of miles in challenging conditions to demonstrate statistical reliability in terms of reductions in fatalities and injuries (1), which could take tens of years of road tests even under the most aggressive evaluation schemes. New methods and metrics are being developed to validate the safety of AV. One possible solution is to use simulation systems, which are common in other domains like law enforcement, defense or medical training. Simulations of autonomous driving can serve two purposes. The first is to test and validate the capability of AV in terms of environmental perception, navigation, and control. The second is to generate a large amount of labelled training data to train machine learning methods, e.g., a deep neural network. The second purpose has recently been adopted in computer vision (2, 3).

The most common way to generate such a simulator is to use a combination of computer graphics, physics-based modeling and robot motion planning techniques to create a synthetic environment in which moving vehicles can be animated and rendered. A number of simulators have recently been developed, such as Intel's CARLA (4), Microsoft's AirSim (5), NVIDIA's Drive Constellation (6), Google/Waymo's CarCraft (7), etc.

While all of these simulators achieve state-of-the-art synthetic rendering results, these approaches are difficult to deploy in the real world. The major hurdle is the need for high-fidelity environment models. The cost of creating life-like CG models is prohibitively high, which means that the synthetic images from these simulators have a distinct, CG-rendered look, i.e. gaming or VR system quality. In addition, the animation of moving obstacles, such as cars and pedestrians, is usually scripted and lacks the flexibility and realism of real scenes. Plus, these systems are unable to generate different scenarios composed of vehicles, pedestrians, or bicycles, as observed in urban environments.

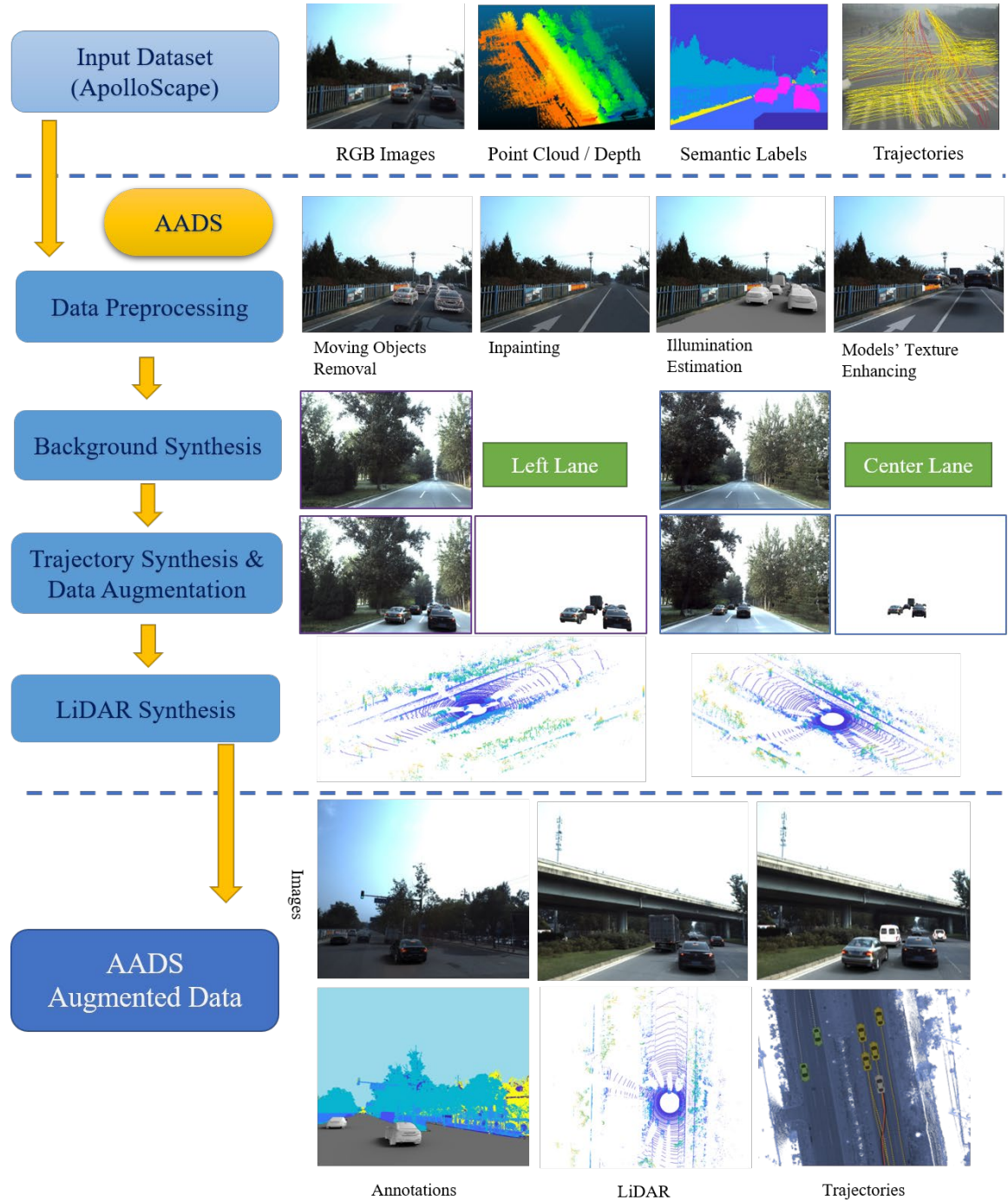


Fig. 1. The inputs, processing pipeline, and outputs of our AADS system. The top is the input dataset. The pipeline of AADS is shown between the dash lines, which contains data preprocessing, novel background synthesis, trajectory synthesis and moving objects augmenting, and LiDAR simulation. The bottom is outputs of AADS system, which include synthesized RGB images, LiDAR point cloud and trajectories with ground true annotations.

In this paper we present a new data-driven approach for end-to-end simulation for autonomous driving: Augmented Autonomous Driving Simulation (AADS). Our method augments real-world pictures with a simulated traffic flow to create photo-realistic simulation scenarios that resemble real-world renderings. Fig. 1 shows the pipeline of our AADS system as well as its inputs and outputs. Specifically, we propose using LiDAR

and cameras to scan street scenes. We decompose the input data into background, scene illumination, and foreground objects. We present a new view synthesis technique to enable changing viewpoints on the static background. The foreground vehicles are fitted with 3D CG models. With accurately estimated outdoor illumination, the 3D vehicle models, computer generated pedestrians, and other movable subjects can be re-positioned and rendered back to the background images to create photo-realistic street view images that look like they were captured from a dashboard camera on a vehicle. Furthermore, the simulated traffic flows, e.g., the placement and movement of synthetic objects, are based on captured real-world vehicle trajectories that look natural and capture the complexity and diversity of real-world scenarios.

Compared with traditional VR-based or game-engine-based AV simulation systems, AADS provides more accurate end-to-end simulation capability without requiring costly CG models or tedious programming to define the traffic flow. Therefore, it can be deployed for large-scale use, including training and evaluation of new navigation strategies for the ego-vehicle.

The key to AADS's success is the wide availability of 3D scene scans and vehicle trajectory data, both of which are needed for the automatic generation of new traffic scenarios. We will also release part of the real-world data that we have collected for the development and evaluation of AADS. These data are either the first of their kind or the largest publicly available in terms of urban scenarios for autonomous driving. The data are fully annotated through a professional labeling service. In addition to AADS, they can also be used for many perceptions and planning related tasks for driving further research in this area.

The technical innovations in this paper include:

- A new data-driven approach for autonomous driving simulation. By using scanned street-view images and real trajectories, both photo-realistic images and plausible movement patterns can be automatically synthesized. This direct scan-to-simulation pipeline, with little manual intervention, enables large-scale deployment to test autonomous cars virtually anywhere and anytime.
- A new set of datasets, including the largest 3D street-view dataset with pixel/point level annotation, and the largest set of traffic trajectories. All of these are captured in metropolitan areas in which the traffic patterns are dense and complex. This kind of dense urban traffic poses significant challenges for autonomous driving.

1.1 Previous Methods

Simulation for autonomous driving (AD) is a very broad topic. Traditionally simulation capabilities have been primarily used in the planning and control phase of AD, e.g., (8–10). More recently, simulation has been used in the entire AD pipeline, from perception and planning to control (see the survey by P. et al. (11)).

While Waymo has claimed that its autonomous vehicle has been tested for billions of miles in their proprietary simulation system, CarCraft (7), little technical detail has been released to the public in terms of its fidelity for training machine learning methods. Researchers have tried to use images from video games to train deep-learning-based perception systems (12, 13).

Recently, a number of high-fidelity simulators dedicated to AD simulation have been developed, such as Intel’s CARLA (4), Microsoft’s AirSim (5), or NVIDIA’s Drive Constellation (6). They allow end-to-end, closed-loop training and testing of the entire AD pipeline beyond the generation of annotated training data. All of these simulators are based on current gaming techniques or engines, which generate high-quality synthetic images in real-time. The limitation of these systems is the fidelity of the resulting environmental model. Even with the state-of-the-art rendering capabilities of these simulators, the resulting images are clearly synthetic, based on computer graphics rendering, and may not provide enough accuracy or details for machine learning methods.

With the availability of LiDAR devices and advances in structure-from-motion, it is now possible to capture large urban scenes in 3D. However, turning the large-scale point cloud into a CG-quality rendered model image is still an on-going research problem. Models reconstructed from these point clouds often lack details or complete textures (14). In addition, AD simulators have to address the problem of realistic traffic patterns and movements. Traditional traffic flow simulation algorithms mainly focus on generating trajectories for cars and vehicles and do not take into account the realistic movement of individual cars or pedestrians. One of the challenges is to simulate realistic traffic patterns, particularly in complex situations when traffic is dense and involves heterogeneous agents (e.g., an intersection scenario with pedestrians in a cross walk).

Our work is related to the approach described by Alhaija et al. (15) in which 3D vehicle models are rendered onto existing captured real-world background images. However, the observation viewpoint is fixed at capture time and the 3D models are chosen from an existing 3D repository that may or may not match those in the real-world images. Their approach can only be used to augment images for machine vision training applications. Overall, ours is the first approach that enables closed loop, end-to-end simulation without the need for environmental modelling or human intervention.

2. Results

2. 1 The Dataset

Since the key idea behind AADS is data-driven, we will first explain the unique datasets we have collected. Some of the datasets have already been released, while some will be released as a part of this paper. We will then show the results for virtual view synthesis and traffic flow generation, the two key components of AADS. Finally, we will evaluate AADS’s effectiveness for autonomous driving simulation. Specifically, we show that the simulated RGB and LiDAR images are useful for increasing the perception performance and the simulated trajectories are useful for increasing the prediction accuracy of obstacle movements—a critical component for the planning and control phases for autonomous cars.

When collecting a dataset, we use a hardware system consisting of two Riegl laser scanners, one real-time line-scanning LiDAR (Velodyne 64-Line), a VMX-CS6 stereo camera system, and a high-precision IMU/GNSS. Using the Riegl scanners, our system can obtain higher-density point clouds with a higher accuracy than the widely used LiDAR scanners. While the VMX-CS6 system provides a wide baseline stereo camera with a high resolution at 3384 * 2710, with the Velodyne LiDAR, we can obtain the shapes and positions of moving objects. To scan a scene, the hardware is calibrated, synchronized, and then mounted on the top of a mid-size SUV that cruises around the

target scene at an average speed of 30km per hour. Note that the RGB images are taken about every one meter.

In our labeling process, we developed a novel labeling pipeline that consists of two stages, 3D labeling and 2D labeling, to make our labeling process accurate and efficient. The basic idea is to use 3D annotations to automatically generate high-quality 2D annotations of static backgrounds/objects in all the image frames by 3D-2D projections. The details of the labeling process can be found in (16).

We annotate 25 different classes covered by five groups in both 3D point clouds and all the image frames. In addition to commonly annotated classes such as car, motorcycle, traffic cone, and so on, we add one new “tricycle” class, representing a popular transport method in East Asian countries. We also annotate 35 different lane markings in both 2D and 3D that are not currently available in existing open datasets. These lane markings are defined based on the color (e.g., white and yellow), type (e.g., solid and broken), and usage (e.g., dividing, guiding, stopping, and parking).

	KITTI	CityScapes	Mapillary	BDD100K	ApolloScape			
Total images	14,999	25,000	25,000	120,000,000	143,906			
Annotated images (bounding-box level)	14,999	no	no	100,000	no			
Annotated images (pixel level)	400	5,000 Fine 20,000 Coarse	25,000	10,000	143,906			
	bounding-box level	pixel level	pixel level	bounding-box level	pixel level			
Scene Complexity (average per image)	person : 0.8 vehicle : 4.1	person : 7.0 vehicle : 11.8	-	person : ~1.3 vehicle : ~11.0	difficulty	easy	moderate	hard
					person	1.1	6.2	16.9
					vehicle	12.7	24.0	38.1
Diversity	day time	day time 50 cities	various weather day & night 6 continents	various weather day & night 4 regions in US	various weather day time 4 regions in China			
3D Annotation	box-level	no	no	no	point-level			
Video Annotation	box-level	no	no	no	pixel-level			
Lane Annotation	no	no	2D / 2 classes	2D / 8 classes	3D / 2D video 28 classes			
Location Accuracy	cm	-	meter	meter	cm			

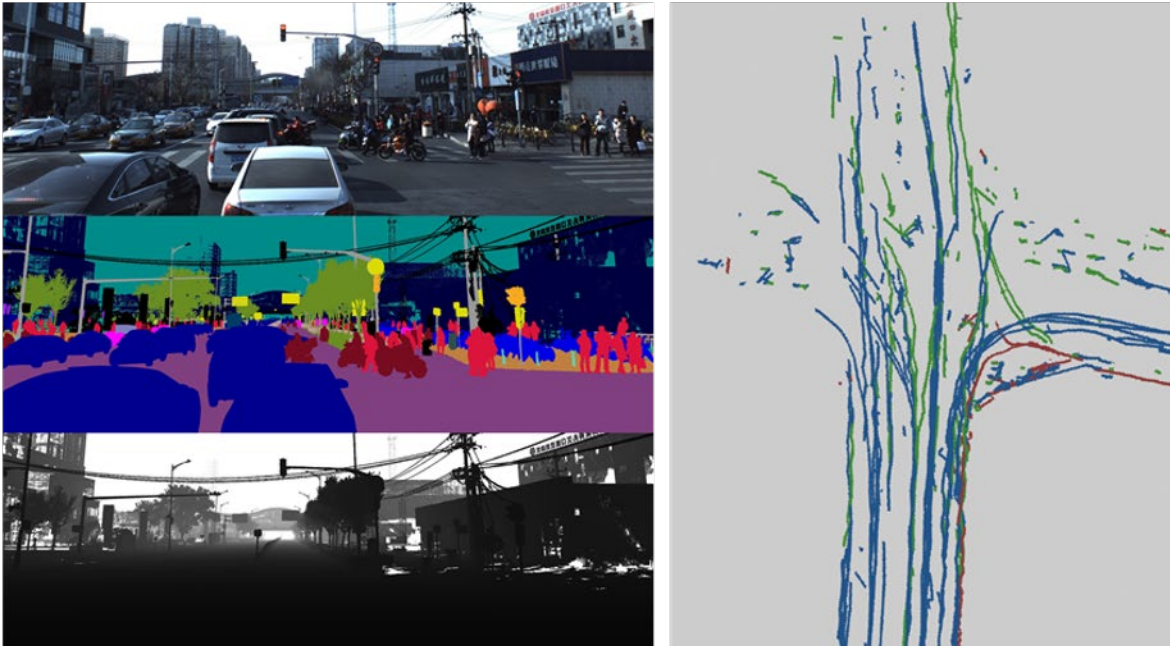


Fig. 2. The ApolloScape dataset and its extension. The top table shows the comparison between ApolloScape and other datasets. The bottom left is RGB images, annotations, and the point cloud, from top to bottom. The bottom right is the labeled traffic trajectories in our dataset.

The table in Fig. 2 shows a comprehensive comparison between our dataset and other street-view datasets in the real world. We find that our dataset outperforms other datasets in many aspects such as scene complexity, number of pixel-level annotations, number of classes, and so on. We have released 143,906 video frames and corresponding pixel-level annotations. We separate the images into three difficulty levels (e.g., easy, moderate, and hard) based on the scene complexities measured by the number of movable objects in an image. Our dataset also contains lots of challenging lighting conditions, such as high-contrast regions due to sunlight and large areas of shadows from the overpass. We name the dataset of RGB images **ApolloScape-RGB**. More importantly, we also provide 3D

point-level annotations on corresponding point could which is not available in any existing street-view datasets, called **ApolloScape-PC**.

In addition to this article, we also announce a new dataset of trajectories named **ApolloScape-TRAJ**. This dataset is a large-scale dataset for urban streets that includes RGB image sequences and trajectory files. It focuses on trajectories of heterogeneous traffic-agents for planning, prediction, and simulation tasks. The dataset includes RGB videos with around 100K 1920×1080 images and 1000km of trajectories for all kinds of moving traffic agents. We use the Apollo acquisition car to collect traffic data and generate trajectories by moving object detection and tracking. In Beijing, we collected trajectory datasets consisting of varying light conditions and traffic densities. The dataset includes many challenging scenarios where vehicles, bicycles, and pedestrians move among one another.

2.2 Evaluations of Augmented Background Synthesis

An important part of our AADS system is synthesizing background images in specific views when running simulations. This ability stems from utilizing the image-based rendering technique and avoids pre-requisite modeling of the full environment.

There exists a vast literature on image-based rendering techniques. However, only a few recent solutions focus on scenes captured with very sparse distributions of images, on which we focus. In other words, we mainly focus on wide baseline image-based rendering for street view scenes: the overlap between left images and right images may be smaller than half the size of the full images. An important part of image-based rendering techniques is obtaining reliable depth. Lots of methods like (17) use the multi-view stereo (MVS) method to estimate depth maps. However, as dataset providing the laser scanned point clouds, we can generate initial depth maps by rendering the point cloud. Initial depth maps are not ready and need to be refined to feed into image-based rendering pipeline. To evaluate our depth refinement method, we use initial depth and refined depth ((b) and (e) in Fig. 3) to synthesize the same novel view. The results are shown in Fig. 3 (f) and (g), respectively. Without depth filtering and completion, the initial depth may have lots of outliers and holes. If we directly use initial depth for rendering, artifacts may occur near the depth holes, e.g., in Fig. 3 (f) and (h), fluctuation will appear in the green rectangle as the view changes, while it's stable in the yellow rectangle.

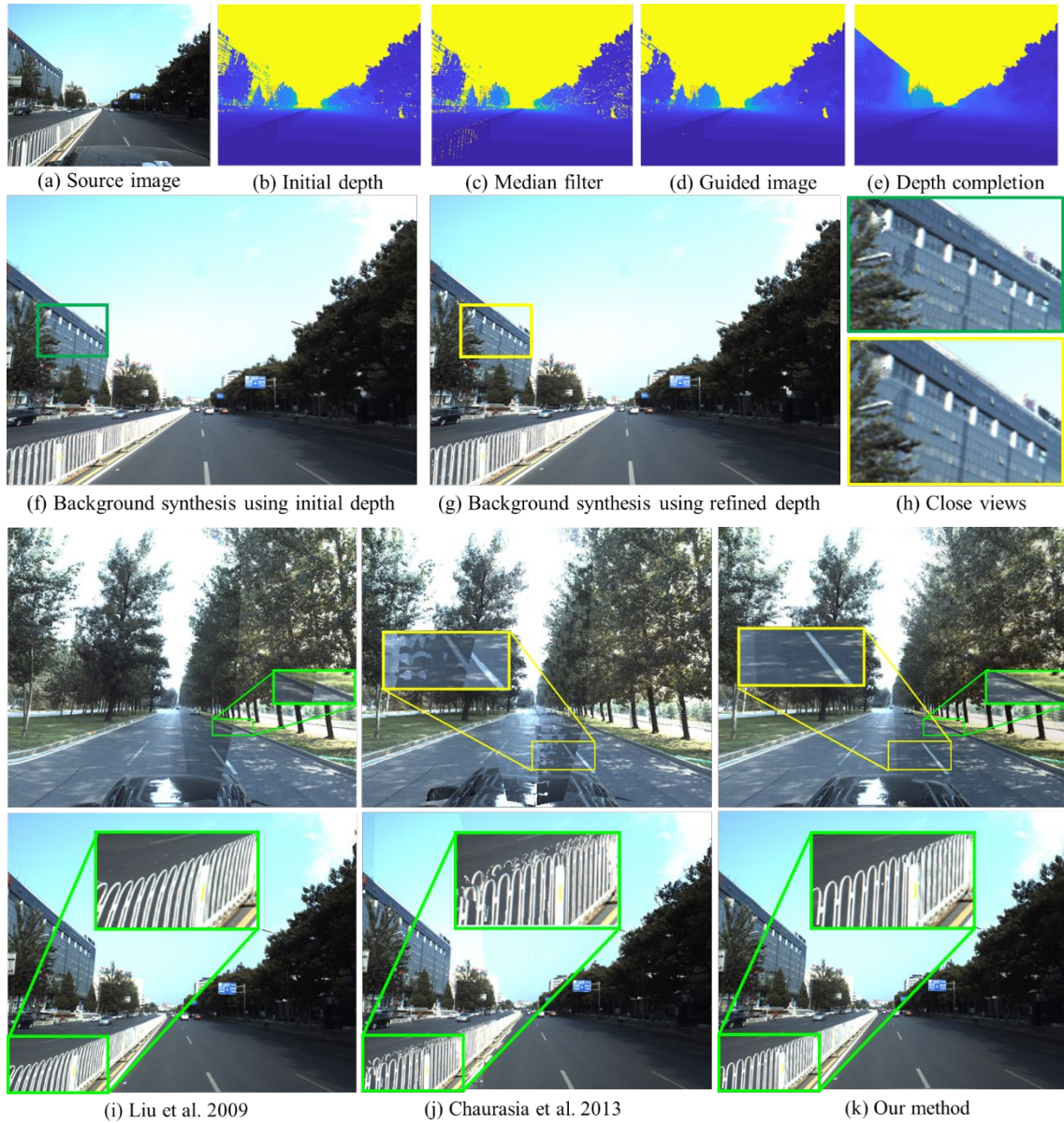


Fig. 3. View Synthesis Result and Effectiveness of Depth Refinement. (a) and (b) The raw RGB and depth images in our dataset, respectively. (c)~(e) The result of depth refinement after filtering and completion. (f) and (g) The result of view synthesis using initial and refined depths with close views in (h). (i)~(k) are the final results of view synthesis using Liu et al.’s method (18), Chaurasia et al.’s method(19), and our method, respectively.

To evaluate our image-based rendering algorithm’s (specifically, the novel view synthesis algorithm) result with refined depths, we compare our method with two typical approaches: the content preserving warping method (Liu et al. (18)) and Chaurasia et al.’s method (19). In the implementation of Chaurasia et al.’s method (19), we use the similarity of super pixels (20) to complete the depth map and perform a local shape-preserving warp on each super pixel.

The synthesis images in Fig. 3 are generated using 4 reference images. The 4 images can be approximately considered as captured in two pairwise parallel views in which the angle of the two optical axes of the pairwise images is small, but the baseline is wide (about

1m). We compare view interpolation and extrapolation with existing methods. As shown in the third row of Fig 3, Liu et al.’s method performs well when the novel view changes are small with respect to the input views. When the distance become larger, view distortion will occur (like the fence in the green rectangular box, the shape of which is deformed illegally). For Chaurasia et al.’s method, ghost artifacts appear when neighboring super pixels are assigned to different or incorrect depths. Our method can get correct depths and preserve the shapes of objects when the novel view changes for both interpolation and extrapolation. In the fourth row of Fig 3, another scene with both a wide baseline and a large rotation angle is evaluated. Because the novel view changes a lot, neither Liu et al.’s method nor Chaurasia et al.’s method may not align well with neighboring reference views. As shown in the figure, curbstones in the green rectangular box and the white road line in the yellow rectangular box have misalignment artifacts. In addition, due to illumination differences that exist in input images, seams are obvious in the results of Liu et al.’s method or Chaurasia et al.’s method. In contrast to those methods, our method can solve both misalignment and seam artifacts.

2.3 Evaluations of Trajectories Synthesis

Another pillar for AADS is its ability to generate plausible traffic flow, particularly when there are interactions between vehicles and pedestrians, e.g., heterogeneous agents who move at different speeds and with different dynamics. This topic is a full research area in its own right, and we have developed new techniques for heterogeneous agent simulations. For the sake of completeness, we briefly show the main result here in Fig. 4. Readers are referred to (21) for more technical details. Specifically, Fig. 4 shows the comparison with ground-truth in input dataset, results of our simulation method and results of Chao et al.’s method (22), which is a state-of-the-art multi-agent simulation approach. In the evaluation, the traffic is simulated on a straight 4-lane road. In our method, the number, positions, and velocities of agents are randomly according to the dataset. We evaluate the comparison using the metric of velocity and minimal distant probability distributions. The metrics are divided into 30 intervals and the probabilities are calculated over all the intervals. As shown in Fig. 4, our simulation results are closer to the input data in both the velocity distribution and the minimal distance distribution.

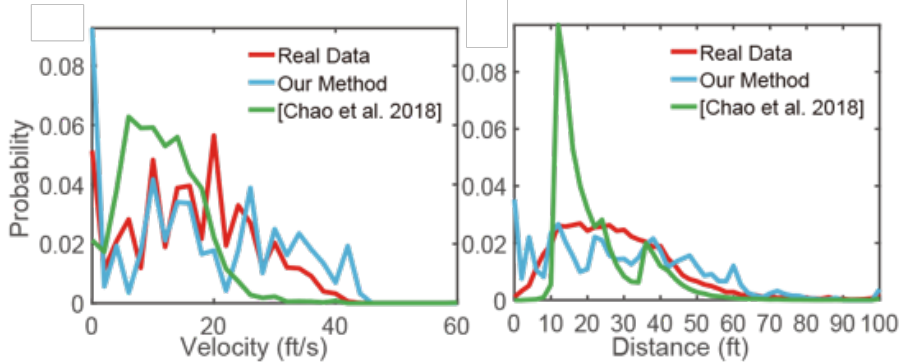


Fig. 4. Comparison of Traffic Synthesis. Velocity and minimal distance distribution of traffic simulation using our method, Chao et al.’s method, and ground truth.

2.4 AADS Evaluations by Autonomous Driving Applications

As shown in Fig. 1, while simulation, our AADS can generate: 1) photo-realistic RGB images with annotation information, such as semantic labels, 3D bounding box, etc.; 2) the augmented LiDAR point cloud; 3) the reasonable traffic flows. Such augmented data are synthesized based on our ApolloScape dataset.

We summarize the evaluations on the AADS simulation output including RGB images, point cloud, and trajectories:

- **AADS-RGB:** For the baseline training set of ApolloScape, we augment the RGB data with AADS and generate the corresponding detection bounding boxes. This dataset is named AADS-RGB and is used to evaluate our RGB synthesis method.
- **AADS-PC:** With our AADS system, we synthesize up to 100k new point cloud frames by simulating the Velodyne HDL-64E S3 LiDAR sensor based on the ApolloScape-PC dataset. The simulated dataset has the same object categories and similar numbers of objects of each kind compared to ApolloScape-PC.
- **AADS-TRAJ:** Our AADS system produces new trajectories based on the ApolloScape-TRAJ dataset. We further evaluate such augmented data using a trajectory prediction method.

2.4.1 Object Detection with AADS-RGB

With respect to evaluations of AADS using autonomous driving applications based on RGB images, we use two large real and two virtual datasets for evaluation: ApolloScape RGB annotated images (ApolloScape-RGB), CityScapes, virtual KITTI (VKITTI), and our simulation data (AADS-RGB).

VKITTI: We use the Virtual KITTI (2) dataset to compare our semi-synthetic simulation method with fully synthetic data. The original dataset comprises 21260 images with different weather and lighting conditions. We random choose 1600 images as a training set. To be fair, during testing we use the Cityscapes dataset to evaluate the models trained with VKITTI and AADS-RGB.

CityScapes: CityScapes (23) is a dataset of urban street scenes. There are 5000 annotated images with fine instance level semantic labels. We use the validation set of 492 images to compare the VKITTI model and the AADS-RGB model.

In this section, we will evaluate the effectiveness of the AADS simulated RGB data. We use the state-of-art objection detection algorithm Mask-RCNN (24) to do the experiments. Considering that we mainly augment cars in the scenes, the results are compared with AP50, AP70, and mean bounding box AP (mAP across threshold at IOU ranging from 0.5 to 0.95 in steps of 0.05) of cars.

In the experiments, AADS-RGB is compared with the VKITTI dataset to show the difference between fully synthetic data and semi-synthetic data.

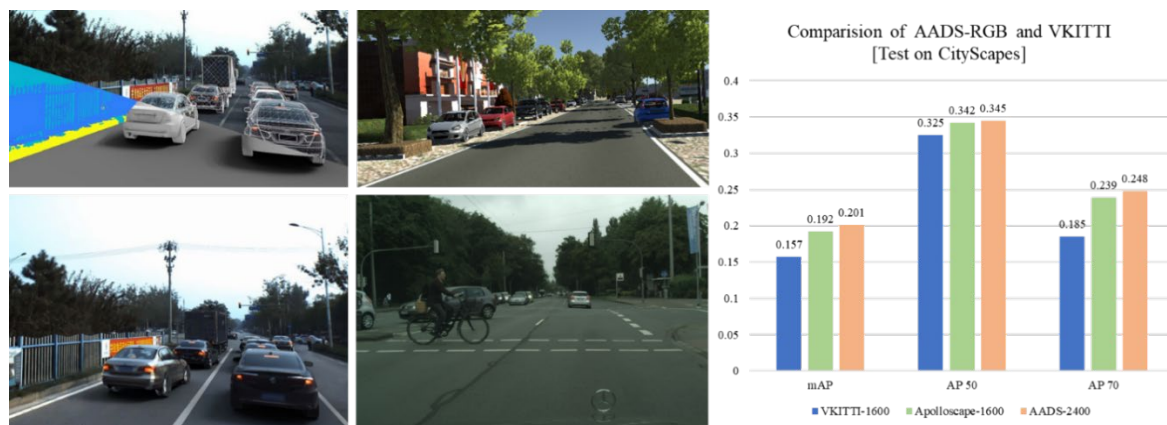


Fig. 5. RGB Object Detection Evaluation. The left column is AADS synthesized RGB images with augmented cars. The middle column contains images from VKITTI (top) and CityScapes (bottom). The table in the right column is the evaluation result.

Synthetic data generation is an easy way to obtain large-scale datasets and has been proven to be effective in autonomous driving. However, the data statistics and distribution limit the capability of virtual data. When applying a model trained with synthetic data to real images, there is a domain gap to eliminate. Our simulation method is built on real background synthesis and a simulated foreground. We assume that this will reduce the domain problem. To verify this assumption, we compare our AADS-RGB dataset with the fully synthetic dataset VKITTI. To be fair, the testing is applied to a third-party dataset.

We train models on VKITTI-1600, ApolloScape-RGB-1600, and AADS-RGB-2400 separately; the suffix shows the number of images used for training. Then the performance is evaluated on the CityScapes validation set. The results are shown in Fig. 5. It can be seen that, due to the domain gap, the metrics of ApolloScape-1600 are higher than those of VKITTI-1600. Note that the image sizes of the images in VKITTI are much smaller than the images in CityScapes or ApolloScape. We therefore apply the VKITTI-1600 model on the downsampled CityScapes to compare. Otherwise, the VKITTI-1600 model tends to miss the large cars and results in worse detections. Adding 800 additional simulated images to ApolloScape-1600 (AADS-RGB-2400) improves the results by roughly one percentage point. This demonstrates that the intrinsic characteristic of our simulation data may be closer to the real data than the full synthetic data.

2.4.2 Detection and Segmentation with AADS-PC

To evaluate AADS point cloud simulations, we use KITTI point cloud datasets (KITTI-PC), the ApolloScape point cloud (ApolloScape-PC), and our simulated point cloud (AADS-PC).

KITTI-PC: The KITTI point cloud dataset consists of 7481 training and 7518 testing frames. These real point cloud frames are labeled corresponding to captured RGB images in the front view. This dataset provides evaluation benchmarks for 1) 2D object detection and orientation estimation; 2) 3D object detection, and 3) bird's eye view evaluations.

Based on those datasets, we evaluate our AADS system on three typical point cloud-based autonomous driving applications: 3D object detection, semantic segmentation and instance segmentation (simultaneous 3D object detection and point cloud segmentation). For those applications, we implement three state-of-the-art algorithms: PointNet++ (25), and the accelerated real-time MV3D (26). The results are evaluated and compared using AP70 (for object detection on KITTI dataset (27)) and mean bounding box/mask AP (for instance segmentation).

data set	car	pedestrian	cyclist	all
100k sim	91.02	72.63	57.21	83.03
16k real	93.27	75.80	62.62	86.33
100k sim +1.6k real	94.10	75.32	61.35	86.40
100k sim+16k real	94.41	79.21	67.01	88.31
100k real	94.39	80.55	67.30	88.50
100k sim+32k real	94.91	80.61	67.51	88.91
100k sim+100k real	95.27	81.20	68.25	89.30

(a)

data set	AP(Bbox)	AP(mask)
16k sim	91.02	72.63
4k real	93.27	75.8
100k sim	94.1	75.32
16k real	94.41	79.21
100k real	94.39	80.55

(b)

Benchmark	real	real + sim
3D detection	54.10%	57.35%
bird's eye view	70.46%	73.19%

(c)

Fig. 6. LiDAR Simulation Evaluations. (a) Evaluation (mean mask AP) results of different datasets for real-time instance segmentation. (b) Evaluations and comparisons with real data in instance segmentation. (c) Car detection (MV3D-LiDAR) on the KITTI benchmark (AP70)

We evaluate the accuracy and effectiveness of the model trained by our simulation data and compare it with the models trained with labeled real data. These simulation and real data were randomly selected from the AADS-PC and ApolloScape-PC datasets, respectively. The mean AP evaluation and comparison results of the instance segmentation models were presented in Fig.6 (b). As shown in Fig. 6 (b), when only trained with our simulation data, the instance segmentation models produce results competitive with the precisely labeled real data. We observed that when using 100k simulation data, the model's performance outperforms 4k real data in both detection and segmentation and very close to 16k or 100k real data. This means that by increasing the size of our produced simulation dataset it can gradually approach the effectiveness of the real dataset.

Next, we use the simulation data to boost the real data (i.e. pre-train the model), as shown in Fig.6(a) and Fig.6(c). This significantly improves (by 2% ~ 4%) the validation accuracy of the original model trained with only the real data. On the ApolloScape-PC dataset, we find that using 100k simulation data to pre-train the model and 1.6k real data for fine-tuning already outperforms the model trained with 16k real data. When fine-tuned with 32k real data, the model already surpassed the one trained with 100k real data. Similarly, on the KITTI benchmarks (Fig.6 (c)), the simulation data helps to improve the detection AP by about 3%. This means that our simulation data helps reduce the quantity demand of the precisely labeled real data to only 10% ~ 20%. With the help of our point cloud simulation system, costs of data labeling are lowered by 80% ~ 90%. More details can be found in (28).

2.4.3 Traffic Predict with AADS-TRAJ

To evaluate the performance of the synthesized cars' trajectories, we adopt Ma's TrafficPredict method (29). This method takes the motion patterns of the traffic-agents in the first T_{obs} frames as input and then predicts their discrete positions in the following T_{pred} frames. In our experiments, T_{obs} is set to 5 and T_{pred} is 7. We extend the real

dataset of 20K frames with an additional 20k simulation data to train the DNN proposed in Ma's method. The metrics of the mean Euclidean distance between the predicted positions and the ground truth positions are used to measure the performance of the trained model. In our case, the average displacement error (mean Euclidean distance of all predicted frames) and the final displacement error (mean Euclidean distance of the $T_{pred-th}$ predicted frame) are adopted. The results in Fig.7 show that prediction error reduces sharply when training with addition 20k simulation data. Considering that most synthesized trajectories in our simulation are cars, the error for cars reduces the most.

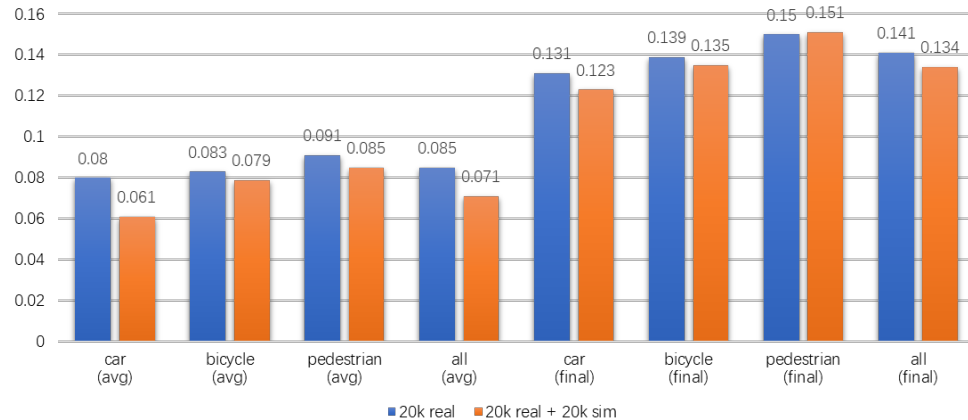


Fig. 7. Traffic Predict Evaluation. Comparison on trajectory prediction with 20k real data and an additional 20k simulation data.

3. Discussion

In the previous section, we showed the effectiveness of AADS for autonomous driving simulation for tasks from perception to planning and control. All of these tasks are achieved by using captured scene data (location specific) and traffic trajectory data (general). The entire pipeline requires very little human intervention. The system can be used to generate a virtually limitless amount of realistic training data with fine annotation or it can be used in-line to simulate the entire AD system from perception to planning to control. The realism and scalability of AADS make it possible to be widely used in any real-world scenarios – as long as the background can be captured.

Compared to VR-based simulations, AADS's viewpoint change for RGB data is limited. Deviating too much from the original captured viewpoints leads to degraded image quality. However, we believe the limited viewing range is actually acceptable for AD simulation. For the most part, a vehicle drives on flat roads and the possible viewpoint changes are limited to rotation and 2D translation on the road plane. There is no need to support a bird's-eye view or a third person perspective for RGB-based perception. Another major limitation of AADS is the lack of lighting/environmental changes (snow/rain) in the scene. These have to be captured for now. However, there are significant advances in image synthesis using generative adversary networks (GANs) (30, 31). Preliminary results synthesizing seasonal changes have been demonstrated. We believe that enabling full lighting/environmental effect synthesis within AADS is a promising direction and we are actively pursuing it now.

4. Materials and Methods

4.1 Data Preprocessing

The mind behind our AADS is utilizing the scanned real images for simulation. Our goal is simulating new vehicles and pedestrians in the scanned scene with new trajectories. To achieve such goal, our AADS should remove the existing moving objects, e.g. vehicles and pedestrians, in scanned RGB images and point cloud before the simulation. However, detecting and removing moving objects is a full research topic in its own area.

Fortunately, most recent datasets provide semantic labels of RGB images even point cloud. In our case, using semantic information in the ApolloScape dataset, we remove objects with specific type, e.g. car, bicycle, and trucks. After moving objects removing, there will definitely appear numerous holes in both RGB images and point cloud, which should be further carefully filled to generate a complete and clean background for AADS. We utilize the most recent RGB image inpainting method (32) to close the holes in images. This method uses the semantic label to guide learning based inpainting technique, which achieve acceptable quality in our case. While the point cloud completion will be later introduced in the depth processing for novel background synthesis (next section).

Given background images, we could place any 3D CG models on the ground and then render into the image space to composite a new simulation image. However, to make the composited image photo-realistic, i.e. looks close to real image, we should first estimate illumination in the background images. This enable our AADS to render 3D CG models with consistent shadows on the ground and the body of vehicles. We solve such outdoor lighting estimation problem according to the method in (33). In addition, to further improve the reality of composited images, our AADS also provides an optional feature to enhancing 3D CG models' appearance by grabbing texture from real images. Specifically, given a RGB image with unremoved vehicles, we retrieve corresponding 3D vehicle models and aligning those models to the input image using method in (34). Similar to (35), we then use symmetric prior to transfer and complete 3D CG models' appearance from aligned image.

4.2 Augmented Background Synthesis

Given the dense point cloud and image sequence produced from automatic scanning, the most straightforward way to build virtual assets for an autonomous driving simulator is to reconstruct the full environment. This line of work focuses on utilizing reconstruction and texture methods to reconstruct complete large-scale 3D models from the scene. However, these methods cannot avoid handcraft editing while modeling. They are always heavy and costly in timing, computation, and even storage.

In this article, we propose a method to synthesize an augmented background in a specific view as needed by a simulator directly when running a simulation. Our method avoids modeling the full scene ahead of running the simulation. Technically, our method creates such a scan-and-simulate system by utilizing the novel view synthesis technique.

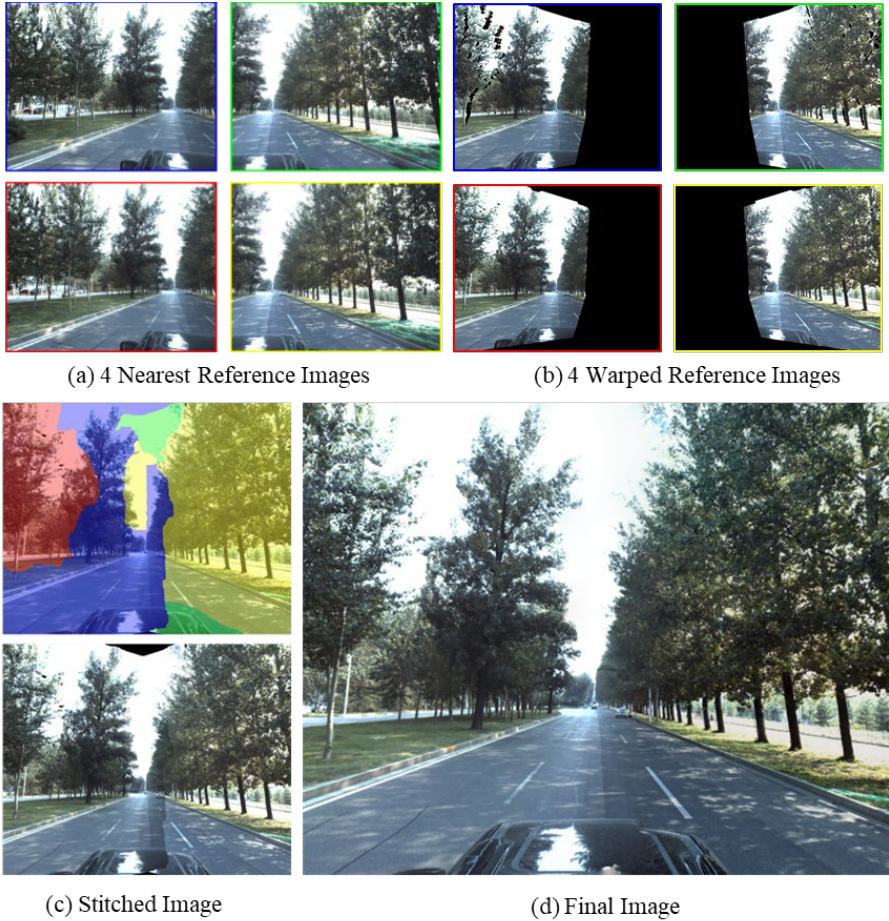


Fig. 8. Novel View Synthesis Pipeline. (a) The 4 nearest reference images are used to synthesize the target view in (d). (b) The 4 reference images are warped into the target view via depth information. (c) A stitching method is used to synthesize the complete image. (d) Final results in the novel view are synthesized after postprocessing, e.g., hole filling and blending.

To synthesize target view, we need first obtain dense depth maps for input reference images. Ideally, those depth maps could be extracted from scanned point cloud. However, such depth maps are always incomplete and not reliable. In our case, the problems come with scanning: (a) The baseline of our stereo camera is small with respect to the size of street view scenes, which leads far objects can only be inferred by very sparse 3D points. (b) The scenes are dynamic with numerous moving vehicles and pedestrians, which will be removed after scanning. However, this leads holes in scanned point clouds; (c) The scenes are always complicated (e.g. many buildings are full covered with glasses), which leads the scanned point clouds incomplete. We solve depth unreliable and incomplete problem using a two steps procedure: depth filtering and depth completion. With respect to depth filtering, we carry out a judiciously selected combination of pruning filters. The first pruning filter is a median filter: a pixel is pruned if its depth value is sufficiently different from the median filtered value. To prevent removing thin structures, the kernel size of median filter is set to small (e.g. 5×5 in our implementation). Then, a guided-filter (36) is applied to keep thin structures and enhance edge alignment between depth map and color image. After having a much more reliable depth, we complete the depth map by propagating the existing depth value to the pixels in holes by solving a first-order Poisson equation, similar to the one used in colorization algorithm (37).

After depth filtering and completion, reliable dense depth maps are obtained, which can provide enough geometry information to render image into virtual views. Similar to (19), given a target virtual view, we select four nearest reference views to synthesize the target view. For each reference view, we first use the forward mapping method to produce a depth map using camera parameters of the virtual view and then perform a depth inpainting to close small holes. Then a backward mapping method and z-test are used to warped the reference color image into the target view. A naïve way to synthesize the target image is blending all warped images together. However, when we blend the warped images using the view angle penalties following article (19), there always exist obvious artifacts. Instead of direct blend warped images together, we solve this problem as an image stitching problem. Specifically, for each pixel in target view's image space, it is optimized to choose color value from one of warped images. This can be formulated as a discrete pixel labeling energy function. We optimize the follow energy for the labelling:

$$\begin{aligned} \arg \min_{\{x_i\}} & \sum_i \lambda_1 E_1(x_i) + \lambda_2 E_2(x_i) + \\ & \sum_{(i,j) \in N} \lambda_3 E_3(x_i, x_j) + \lambda_4 E_4(x_i, x_j) + \lambda_5 E_5(x_i, x_j) \end{aligned} \quad (1)$$

Here, x_i is the i -th pixel and N is the set of surrounding pixels. $E_1(x_i)$ is the data term for one pixel. We use view angle penalty in article (38) to define $E_1(x_i)$. But in our street view scene, depths of lots pixels are so far that the angle view penalties are almost the same (near zero), which cannot be used to choose the best warped image. To solve this problem, when angle view penalties are zero, we use camera position to find the nearest warped image to the synthesized view and rise its weight. $E_1(x_i)$ is defined as $E_1(x_i) = E_{angle}(x_i)W_{label}(x_i)$. Here, $E_{angle}(x_i)$ is view angle penalty calculated in (38).

$W_{label}(x_i) = D_{pos}(C_{x_i}, C_{syn})D_{dir}(C_{x_i}, C_{syn})$ is the distance between the reference view and target view, where D_{pos} represents the distance of camera positions and D_{dir} is the angle between optical axes of the two cameras.

$E_2(x_i)$ is the occlusion term used to exclude the occlusion areas while minimizing the pixel labeling energy. Occlusion often occurs near depth edges. Thus, when using the backward mapping method to render the warped images, we could detect the occlusion by testing depth values. All pixels with depth values larger than the source depth in reference view form an occlusion mask, which is then used to define $E_2(x_i)$. Specifically, when an occlusion mask is invalid, i.e. this pixel is non-occlusion, we set $E_2(x_i) = 0$ to add no penalty into the energy function. When a pixel is occluded, we set $E_2(x_i) = \infty$ to exclude this pixel completely.

The rest of the terms in Eq.1 are smoothness terms: color term $E_3(x_i, x_j)$, depth term $E_4(x_i, x_j)$, and color gradient term $E_5(x_i, x_j)$. Similar to (39), the color term $E_3(x_i, x_j)$ is defined by a truncated seam-hiding pairwise cost first introduced in (40): $E_3(x_i, x_j) = \min(\|c_i^{x_i} - c_i^{x_j}\|^2, \tau_c) + \min(\|c_j^{x_i} - c_j^{x_j}\|^2, \tau_c)$. Similarly, the depth term $E_4(x_i, x_j)$ is defined as: $E_4(x_i, x_j) = \min(|d_i^{x_i} - d_i^{x_j}|, \tau_d) + \min(|d_j^{x_i} - d_j^{x_j}|, \tau_d)$, where the

truncation thresholds are set to $\tau_c = 0.5$, $\tau_d = 5\text{m}$ in our implementation. Because illumination difference may occur between different reference images, color difference is not sufficient to ensure a good stitch. An additional gradient difference $E_5(x_i, x_j)$ is used, and we expected the gradient vector to be similar on both sides of the seam. $E_5(x_i, x_j) = |g_i^x - g_j^x| + |g_i^y - g_j^y|$.

The term weights in Eq. 1 are set to $\lambda_1 = 200$, $\lambda_2 = 1$, $\lambda_3 = 200$, $\lambda_4 = 100$, and $\lambda_5 = 50$. The labeling problems are solved using the TRW-S method (41). Fig. 8 shows the pipeline and results of augmented background synthesis. Note Fig. 8 (c), color difference may exist near the stitching seams after image stitching. To get consistent results, a modified Poisson image blending method (42) is performed. Specifically, we select the nearest reference image as the source domain and then fix its edges to propagate color brightness to the other side of stitch seams. After solving the Poisson equation, we get the fusion result shown in Fig. 8 (d). Note that, when the novel view is far away from any input views, e.g., large view extrapolation, dis-occluded regions will appear and cannot find corresponding areas from the input images. We mark those regions as holes and set their gradient value to zero. Thus, these holes will be filled with plausible blurred color when solving the Poisson equation.

4.3 Moving Objects Synthesis and Data Augmentation

With a synthesized background image in the target view, a complete simulator should also synthesize realistic traffics with diverse moving objects (e.g., vehicles, bicycles, pedestrians) and produce corresponding semantic labels and bounding boxes in images and simulated LiDAR point clouds.

We solve the traffic generation problem using the data-driven method described in (22). Specifically, given the localization information, we first extract the lane information from an associated HD map. Then we randomly initialize the moving objects' positions within the lanes and ensure that the moving objects' directions are reasonable based on the containing lanes. We use agents to simulate the moving objects' movements under constraints such as avoiding collisions and yielding to pedestrians. The multi-agent system is iteratively deduced and optimized using previously captured traffics following a data-driven method to produce moving objects' positions and directions in each frame. With respect to the image synthesis, we render 3D models using the traffic information and generated annotated data using the physical rendering engine PBRT (43).

4.4 LiDAR Synthesis

Regard to the LiDAR point clouds synthesis, a method to produce realistic point clouds compared to specific LiDAR sensor (e.g., Velodyne HDL-64E S3) is not trivial. A real LiDAR sensor captures the surrounding scene by judging the time of flight for laser pulses emitted from the LiDAR and then reflected from target surfaces (44). A point is generated if the returned pulse energy of a laser beam is big enough. We model the behavior of laser beams to simulate this physical process. Specifically, the emitted laser beam could be modeled using parameters including the vertical and azimuth angles and their angular noises, as well as the distance measurement noise. For example, the Velodyne HDL-64E S3 emits 64 laser beams in different vertical angles ranging from -24.33° to 2° . During data acquisition, HDL-64E S3 rotates around its own upright direction and shoots laser beams at a predefined rate to accomplish 360° coverage of the scenes. Ideally, these

parameters should remain constant with respect to the type of LiDAR sensor. However, in experiments we found that those parameters vary sharply among devices. To be closer to reality, we obtain these values statistically from real point clouds.

Specifically, we collect real point clouds from these HDL-64E S3 sensors on top of parked vehicles, guaranteeing the point curves generated by different laser beams are smooth. The points of each laser beam are then marked manually and fitted by a cone with the apex located in the LiDAR center. The half-angle of the cone minus $\pi/2$ forms the real vertical angle, while the noise variance is determined from the deviation of lines constructed by the cone apex and the points from the cone surface. The real vertical angles usually differ from the ideal ones by 1° - 3° . In our implementation, we model the noise with Standard Gaussian Distribution, setting the distance noise variance to 0.5cm and the azimuth angular noise variance to 0.05° . Our experiments prove that real parameter values significantly boost the DNN performance.

To generate a point cloud, we have to compute intersections of laser beams and the virtual scene. For this we propose a cube map-based method to handle the hybrid data of virtual scenes, e.g., points and meshes. Instead of computing intersections between beams and the hybrid data, we compute the intersection with the projected maps (e.g., depth map) of scenes, which offer the equivalent information but in a much simpler form. We'd like to highlight that our LiDAR simulation method can be easily extended for arbitrary LiDAR sensors and any sensor solution for different numbers and poses of sensors.

References and Notes

1. N. Kalra, S. M. Paddock, “Driving to Safety: How Many Miles of Driving Would It Take to Demonstrate Autonomous Vehicle Reliability?” (RAND Corporation, 2016).
2. A. Gaidon, Q. Wang, Y. Cabon, E. Vig, Virtual worlds as proxy for multi-object tracking analysis, in *Proc. of the IEEE Conference on Computer Vision and Pattern Recognition (CVPR)* (2016).
3. M. Müller, V. Casser, J. Lahoud, N. Smith, B. Ghanem, Sim4CV: A photo-realistic simulator for computer vision applications, *International Journal of Computer Vision*, 1–18 (2018).
4. A. Dosovitskiy, G. Ros, F. Codevilla, A. Lopez, V. Koltun, CARLA: An open urban driving simulator, in *Proceedings of the 1st Annual Conference on Robot Learning* (2017), pp. 1–16.
5. S. Shah, D. Dey, C. Lovett, A. Kapoor, Airsim: High-fidelity visual and physical simulation for autonomous vehicles, in *Field and Service Robotics* (2017); <https://arxiv.org/abs/1705.05065>.
6. NVIDIA, *NVIDIA DRIVE CONSTELLATION: Virtual Reality Autonomous Vehicle Simulator* (2017).
7. A. C. Madrigal, *Inside Waymo’s Secret World for Training Self-Driving Cars* (2017).
8. M. Likhachev, D. Ferguson, Planning long dynamically feasible maneuvers for autonomous vehicles. *The International Journal of Robotics Research*. **28**, 933–945 (2009).

9. S. J. Anderson, S. C. Peters, T. E. Pilutti, K. Iagnemma, Design and development of an optimal-control-based framework for trajectory planning, threat assessment, and semi-autonomous control of passenger vehicles in hazard avoidance scenarios, in *Robotics Research* (Springer, 2011), pp. 39–54.
10. C. Katrakazas, M. Quddus, W.-H. Chen, L. Deka, Real-time motion planning methods for autonomous on-road driving: State-of-the-art and future research directions. *Transportation Research Part C: Emerging Technologies*. **60**, 416–442 (2015).
11. S. D. Pendleton *et al.*, Perception, planning, control, and coordination for autonomous vehicles. *Machines*. **5**, 6 (2017).
12. M. Johnson-Roberson *et al.*, Driving in the matrix: Can virtual worlds replace human-generated annotations for real world tasks? *arXiv preprint arXiv:1610.01983* (2016).
13. S. R. Richter, V. Vineet, S. Roth, V. Koltun, Playing for data: Ground truth from computer games, in *European Conference on Computer Vision* (Springer, 2016), pp. 102–118.
14. H. Lin *et al.*, Semantic Decomposition and Reconstruction of Residential Scenes from LiDAR Data. *ACM Transactions on Graphics, (Proc. of SIGGRAPH 2013)*. **32** (2013).
15. H. A. Alhaija, S. K. Mustikovela, L. Mescheder, A. Geiger, C. Rother, Augmented reality meets computer vision: Efficient data generation for urban driving scenes. *International Journal of Computer Vision*. **126**, 961–972 (2018).
16. X. Huang *et al.*, The ApolloScape Dataset for Autonomous Driving. *arXiv preprint arXiv:1803.06184* (2018).
17. E. Penner, L. Zhang, Soft 3D reconstruction for view synthesis. *ACM Transactions on Graphics (TOG)*. **36**, 235 (2017).
18. F. Liu, M. Gleicher, H. Jin, A. Agarwala, Content-preserving warps for 3D video stabilization, in *ACM Transactions on Graphics (TOG)* (ACM, 2009), vol. 28, p. 44.
19. G. Chaurasia, S. Duchene, O. Sorkine-Hornung, G. Drettakis, Depth synthesis and local warps for plausible image-based navigation. *ACM Transactions on Graphics*. **32**, 1–12 (2013).
20. R. Achanta *et al.*, SLIC superpixels compared to state-of-the-art superpixel methods. *IEEE transactions on pattern analysis and machine intelligence*. **34**, 2274–2282 (2012).
21. J. Ren *et al.*, Heter-Sim: Interactive data-driven optimization for simulating heterogeneous multi-agent systems. *arXiv preprint arXiv:1812.00307* (2018).
22. Q. Chao, Z. Deng, J. Ren, Q. Ye, X. Jin, Realistic Data-Driven Traffic Flow Animation Using Texture Synthesis. *IEEE Transactions on Visualization & Computer Graphics*, 1167–1178 (2018).
23. M. Cordts *et al.*, The Cityscapes Dataset for Semantic Urban Scene Understanding, in *Proc. of the IEEE Conference on Computer Vision and Pattern Recognition (CVPR)* (2016).

24. K. He, G. Gkioxari, P. Dollár, R. Girshick, Mask r-cnn, in *Computer Vision (ICCV), 2017 IEEE International Conference on* (IEEE, 2017), pp. 2980–2988.

25. C. R. Qi, L. Yi, H. Su, L. J. Guibas, Pointnet++: Deep hierarchical feature learning on point sets in a metric space, in *Advances in Neural Information Processing Systems* (2017), pp. 5099–5108.

26. X. Chen, H. Ma, J. Wan, B. Li, T. Xia, Multi-view 3D Object Detection Network for Autonomous Driving, in *2017 IEEE Conference on Computer Vision and Pattern Recognition (CVPR)* (2017), pp. 6526–6534.

27. A. Geiger, P. Lenz, R. Urtasun, Are we ready for autonomous driving? the kitti vision benchmark suite, in *2012 IEEE Conference on Computer Vision and Pattern Recognition (CVPR)* (2012), pp. 3354–3361.

28. J. Fang *et al.*, Simulating LIDAR Point Cloud for Autonomous Driving using Real-world Scenes and Traffic Flows. *arXiv preprint arXiv:1811.07112* (2018).

29. Y. Ma *et al.*, TrafficPredict: Trajectory Prediction for Heterogeneous Traffic-Agents. *arXiv preprint arXiv:1811.02146* (2018).

30. P. Isola, J.-Y. Zhu, T. Zhou, A. A. Efros, Image-to-image translation with conditional adversarial networks. *arXiv preprint* (2017).

31. T.-C. Wang *et al.*, High-Resolution Image Synthesis and Semantic Manipulation with Conditional GANs, in *Proceedings of the IEEE Conference on Computer Vision and Pattern Recognition* (2018).

32. Y. Song *et al.*, SPG-Net: Segmentation Prediction and Guidance Network for Image Inpainting. *arXiv preprint arXiv:1805.03356* (2018).

33. Y. Liu, X. Qin, S. Xu, E. Nakamae, Q. Peng, Light source estimation of outdoor scenes for mixed reality. *The Visual Computer*. **25**, 637–646 (2009).

34. M. Corsini, M. Dellepiane, F. Ponchio, R. Scopigno, Image-to-Geometry Registration: a Mutual Information Method exploiting Illumination-related Geometric Properties, in *Computer Graphics Forum* (Wiley Online Library, 2009), vol. 28, pp. 1755–1764.

35. N. Kholgade, T. Simon, A. Efros, Y. Sheikh, 3D object manipulation in a single photograph using stock 3D models. *ACM Transactions on Graphics*. **33**, 1–12 (2014).

36. K. He, J. Sun, X. Tang, Guided image filtering. *IEEE transactions on pattern analysis and machine intelligence*. **35**, 1397–1409 (2013).

37. A. Levin, D. Lischinski, Y. Weiss, Colorization using optimization, in *ACM transactions on graphics (tog)* (ACM, 2004), vol. 23, pp. 689–694.

38. C. Buehler, M. Bosse, L. McMillan, S. Gortler, M. Cohen, Unstructured lumigraph rendering, in *Proceedings of the 28th annual conference on Computer graphics and interactive techniques* (ACM, 2001), pp. 425–432.

39. P. Hedman, S. Alsisan, R. Szeliski, J. Kopf, Casual 3D photography. *ACM Transactions on Graphics*. **36**, 1–15 (2017).
40. V. Kwatra, A. Schödl, I. Essa, G. Turk, A. Bobick, Graphcut textures: image and video synthesis using graph cuts, in *ACM Transactions on Graphics (ToG)* (ACM, 2003), vol. 22, pp. 277–286.
41. V. Kolmogorov, Convergent tree-reweighted message passing for energy minimization. *IEEE transactions on pattern analysis and machine intelligence*. **28**, 1568–1583 (2006).
42. P. Pérez, M. Gangnet, A. Blake, Poisson image editing. *ACM Transactions on graphics (TOG)*. **22**, 313–318 (2003).
43. M. Pharr, W. Jakob, G. Humphreys, *Physically based rendering: From theory to implementation* (Morgan Kaufmann, 2016).
44. S. Kim, I. Lee, Y. J. Kwon, Simulation of a Geiger-mode imaging ladar system for performance assessment. *sensors*. **13**, 8461–8489 (2013).

Acknowledgments

Author contributions: The project was conceived by Rg. Y.. W. L. and Cw. P. developed the concept and systems. Jp. R. developed the trajectory synthesis framework. R. Z. and Qc. G. performed synthesized RGB image evaluations. Xy. H. helped collecting RGB and point cloud datasets. J. F. and Fl. Y. performed synthesized LiDAR point cloud evaluations. Yx. M. helped collecting trajectories dataset and performed simulated trajectory evaluations. Gp. W., Ww. X. and Hj. G. discussed the results and contributed to the final manuscript. The paper was written by W. L., D. M. and Rg.Y..

Competing interests: The authors declare that they have no competing interests.

Data and materials availability: The RGB and point cloud datasets (ApolloScape-RGB and ApolloScape-PC) are hosted with the web link <http://apolloscape.auto/scene.html>. While, the trajectory dataset (ApolloScape-TRAJ) announced along with this paper can freely download through link <http://apolloscape.auto/trajectory.html>. The high-resolution video can also be watched through <https://youtu.be/Y2ha9gE0pYw>.